# Optically Inducing and Probing the Local Crystallization of Ultra-Thin Gesbte Films by Single-Pulse Laser Irradiations

Mania Majumder, Walter Batista-Pessoa, Catalin Constantinescu, Mathieu Koudia, Elisa Petroni, Yannick Le-Friec, Mathieu Abel, Isabelle Berbezier, David Grojo

# Optically inducing and probing the local crystallization of ultra-thin GeSbTe films by single-pulse laser irradiations

Mania Majumder[a], Walter Batista-Pessoa[b], Nicolas Bottin[a,b,c], Catalin Constantinescu[a], Mathieu Koudia[b], Elisa Petroni[d], Yannick Le-Friec[c], Mathieu Abel[b], Isabelle Berbezier[b], David Grojo*[,a]

[a] *Aix-Marseille University, CNRS, LP3 UMR 7341, Marseille, 13009, France*
[b] *Aix-Marseille University, CNRS, IM2NP UMR 7334, Marseille Cedex 20, 13397, France*
[c] *STMicroelectronics, 850 Rue Jean Monnet, Crolles, 38920, France*
[d] *STMicroelectronics, Camillo Olivetti, 2, Agrate Brianza MB, 20864, Italy*

**Abstract**

Technology advances on phase change memories based on GeSbTe alloys rely on complex material analyses in extremely miniaturized electrical devices and so require numerous and tedious tasks. In this work, we optically emulate and measure the phase change of GeSbTe alloys without the need for device integration. Using microsecond laser pulses, we crystallize multilayer thin-film systems. The irradiated materials are then investigated using microscopy and spectroscopy methods. By comparing measurements with optical simulations, we demonstrate that quantitative descriptions are achievable and thus that local phase changes of ultrathin films can be directly monitored. An improved detection sensitivity is found for the infrared region of the spectrum leading to the use of a transmission microscopy arrangement operated at 1200-nm wavelength for *insitu* studies. With appropriate laser conditions under damage threshold, we demonstrate the ability of the pulses to selectively crystalize $Ge_2Sb_2Te_5$ layers while leaving untouched other germanium-rich layers due to distinct crystalization temperatures. The optical detection scheme is shown to detect phase changes of single ultrathin films with thicknesses as small as 5 nm. This opens a way for all-optical methods complementing advanced material analyses for GeSbTe material studies and the development of the next generations of phase change memories.

*Keywords:* laser-matter interaction, multilayer thin films, crystallization, phase change materials, optical microscopy, spectroscopy.

## 1. Introduction

In the 60's, S. R.Ovshinsky *et al.* made a scientific breakthrough when they first observed a fast and reversible switching effect in the STAG ($Si_{12}Te_{48}As_{30}Ge_{10}$) composition [1]. This demonstration of unique phase change properties was the foundation of optical disk technologies and phase change memories (PCM). After decades of investigations of various alloys of phase change materials, it becomes evident that $Ge_2Sb_2Te_5$ alloy stands out. It is today a widely employed material in PCM devices because of its ultrafast switching time [2] (in the order of nanoseconds or less) and long-term stability [3] (exceeding years). A large number of switching cycles between $10^5$ and $10^{12}$ depending on configurations [4] are also demonstrated ensuring reliable and durable memory storage. The properties are crucial for upholding the integrity of the stored data and the performance of the device. In particular, the GeSbTe alloy (GST) composition and technology configuration is actually a major concern for industrial applications.

In PCMs, the optimized amplitude and duration of the applied electrical pulses lead to the reversible phase-switching effect resulting in a drastic change in the local electrical properties which is the basis for information storage. Information is basically stored as low-resistivity crystalline memory points, erasable through local re-amorphization of the matrix. While re-amorphization is a rapid process, the crystallization process is comparatively slow, imposing constraints on the data transfer rate. Despite the ease of implementing electrical switching in commercial devices, challenges like impedance mismatch and non-uniform phase change distribution in GST materials, attributed to uneven joule heating, can impede the speed and reliability of this switching process [5]. As evidenced by optical disk technologies based on similar materials, the phase change of the material does not only significantly affect the electrical characteristics (resistivity), but important variations in the optical properties (reflectivity or transmittivity) are also highly expected even for electrical device configuration. This gives the vision of this work aiming at developing an all-optical method for studying PCM materials.

In relation with this vision, the most important experimental parameter in laser annealing experiments is the applied laser fluence which is the energy density per pulse on the target (in $J/cm^2$). At low fluence levels, the material's structure remains unchanged, as the delivered energy is insufficient to induce alterations. Conversely, at high fluence, one can easily observe ablation and the removal of the material surface, attributed to the excessive energy imparted [6]. Reversible phase change occurs in intermediate regimes between these two con-

ditions. Concentrating on past research involving laser experiments on GST materials, it is interesting to note that numerous groups investigated the laser response, in space and time, of $Ge_2Sb_2Te_5$ in different configurations [7, 8, 9, 10, 11, 12, 13, 14, 15, 16, 17]. However, despite these efforts, extracting a comprehensive picture of the response to laser radiation remains challenging. The complexity arises from variations in sample compositions, thicknesses, and laser irradiation conditions (laser wavelength, fluence, repetition rate, and number of applied pulses) as well as the use of diverse characterization techniques, often sensitive to different properties. Moreover, some of these works focus on the use of extremely short laser pulses with durations down to the femtosecond regime and so inducing dynamical processes significantly faster than those in real memory devices. The high intensity inherent to these pulses potentially induces non-thermal responses [18] leading to material transformations which are hardly representative of PCM device conditions. Laser annealing with longer pulses is however expected to achieve pure-thermal stimulation representative to technological conditions.

In this article, we investigate multilayer GST systems annealed using microsecond laser pulses. The pulses are expected to induce purely thermal conditions favorable to achieve phase transitions from amorphous to crystallized states with micrometer spatial control. Using different optical characterization techniques including spectroscopy and microscopy techniques, we identify the spectral domains and optical probing methods which are the most sensitive to detect the crystallization process in ultrathin films. From this, we develop an operational laser setup capable of locally inducing and *in situ* probing the phase change of GST thin films. The quantitative agreement between the measurements and predicted optical signature demonstrates an all-optical tool to study phase change responses depending on material compositions and layer arrangements. This can serve to directly identify the most promising material configurations for technological considerations.

## 2. Experimental techniques

### 2.1. Studied samples

In this work, we do not consider spatial configurations directly corresponding to PCM devices made of individual cells scaled down to the nanoscale in the three dimensions for high density information storage. Instead, we study one-dimensional thin-film GST systems made of distinct layers with different compositions in order to address Materials Science questions relevant for technology developments.

All our studied thin-film samples are supported by 700 µm thick silicon (001) substrates (both sides polished) and the investigated GST materials are grown by sputtering method using an industrial Physical Vapor Deposition (PVD) reactor. We prepare GST layers with stoichiometry close to $Ge_2Sb_2Te_5$ and Ge-rich GST alloys (hereafter called GGST). The Ge concentration in GGST layers is > 50%. According to the thermodynamic phase diagram, amorphous $Ge_2Sb_2Te_5$ first transforms into a metastable face-centered cubic (fcc) at $\sim$ 150°C, then to a compact hexagonal (hcp) defected phase at $\sim$ 430-450°C. Recently it has been shown that GGST compared to GST can be beneficial to provide lower crystallization rates and higher phase change temperature of approximately 350°C [19]. However, in real memory devices, the kinetics of amorphization/crystallization of GST materials involves fast dynamical processes very different from those in thermodynamic steady state. Long thermal annealing (using a furnace) can then serve for comparisons between various chalcogenide alloys, but cannot give the understanding of the material responses in real fast annealing conditions. The short-pulse laser annealing method proposed here is then expected to be more representative to technological conditions and must offer an opportunity to confirm different crystallization threshold conditions depending on alloy compositions.

Thanks to a limited thermal budget during the deposition process, the studied films are initially almost fully amorphous as confirmed by transmission electron microscopy (TEM) analyses. For this academic study, we have used GGST materials also doped with nitrogen (N), by choosing among all the different available dopings (N, C, As, In), that are commonly known as beneficial for PCM. From literature, it is known that the introduction of N-doping significantly restrains the crystallization of Ge, hinders the diffusion of Ge within GST-based alloys due to the development of robust Ge-N bonds, and also reduces the average grain size of the resulting crystallized phases [20, 21].

Three types of samples involving GST and GGST layers of total thickness $t$ varying from 50 to 150 nm were prepared for this work. The characteristics of the studied samples are summarized in Table-1. The first type of sample (Type-1) comprises a thick GGST layer with thickness corresponding to 90% of the total thickness $t$, while a GST thin film is sandwiched between this layer and the substrate. The second type (Type-2) implies the same material compositions but in a multilayer configuration. It features a stack of 10 layers based on a thin GST and GGST layer combination repeated five times. The sensitivity of optical methods obviously depends on film thicknesses. With these choices, we can compare samples of

| Samples | Type-0 | Type-1 | Type-2 |
|---|---|---|---|
| Capping layer | None | TiN | TiN |
| Layers | 0.9$t$ GGST, 0.1$t$ GST | 0.9$t$ GGST, 0.1$t$ GST | Stack of 10 layers (0.1$t$ GST + 0.1$t$ GGST repeated 5 times) |
| Substrate | Si | Si | Si |

Table 1: Characteristics of different types of studied multilayer GST samples of different total thicknesses $t$. The description includes the thickness values for GST and Ge-enriched GST (GGST) layers according to the compositions described in the text. The substrate is identical for all samples and the presence or not of a protective layer (capping) is mentioned for the different types of samples.

identical thicknesses $t$. As we will see later on, the important difference in relative proportion between GGST and GST exhibiting very different threshold conditions for crystallization gives us also the possibility to assess the sensitivity of the optical detection methods applied to extremely thin films. In particular, the presented results concentrate on the samples with $t = 50$ nm and so allow stying the sensitivity down to 5 nm GST.

Another important aspect to consider was the possible oxidation of the films that may cause difficulties for reproducible results according to studies showing a dependence of the oxidation degree for the crystallization temperature of GGST [22]. For this reason, Type-1 and Type-2 samples are capped with a 21-nm protective layer of TiN (*insitu* deposited). In addition to improved sample stability, TiN gives another advantage as it is strongly absorbing at the laser wavelength used for this work (1.07 µm). According to the absorption coefficient for sputtered TiN films measured [23] at $\alpha \approx 6.5 \times 10^5$ cm$^{-1}$ (much higher than for GST materials) the corresponding penetration depth ($\sim$ 15 nm) is under the thickness of the TiN thin layer. In this way the heat source applied to the system and controlled by laser irradiation is confined in this layer and thus can be considered as identical for both types of samples which would not be the case without capping. Despite this simplification, one should not ignore to account for the optical response of TiN in the applied diagnostics. This may raise also questions for potential screening effects from this layer limiting the sensitivity of optical methods to monitor transformations in the underneath GST layers. This is the reason why the study integrates also comparisons with another type of sample named Type-0, strictly identical to Type-1 but without the TiN film.

### 2.2. Laser irradiation set-up and optical diagnostics

The experimental arrangement developed for initiating laser-induced modification of the GST films is schematically depicted in Figure 1. The samples are exposed to laser irradiation in ambient air using a source (IPG, YLR-150/1500-QCW-AC) operating in a so-called quasi-continuous wave (QCW) regime at a central wavelength of 1070 nm. In practice, its integrated electronics gates a continuous emission to deliver pulses of 50-µs minimal duration. The laser beam irradiates the sample at an angle of incidence of $\sim 28°$. The angle of incidence of the laser beam on the sample is precisely controlled using two mirrors (see M1 and M2 in Figure 1). A focusing lens (L) of 1-m focal length is used and its position is adjusted so that the sample is about 6.5 cm prior to the geometrical focal plane and the elliptical spot exhibits a size of $> 300$ µm on the sample surface (defocused plane). For precise determination of the applied Gaussian fluence profiles the elliptical spot is characterized using a CCD camera positioned in the same plane as the sample surface (repositioning method described hereafter). The vertical size is measured at $\sim 340$ µm (beam waist $w_0$ that is the radius at $1/e^2$ of maximum intensity) and a very modest ellipticity is found. This corresponds relatively well with the expected effect from the angle of incidence ($\sim$ 13%). Given the excellent agreement of the measured horizontal and vertical

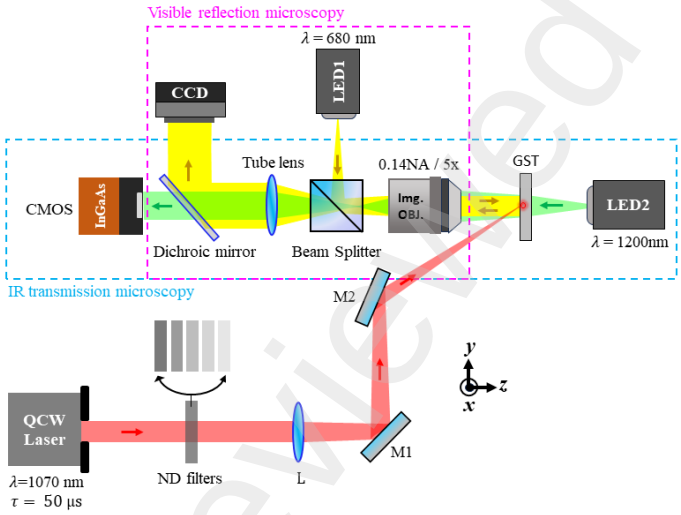


Figure 1: Schematic diagram of the experimental setup designed for annealing studies on GST. It combines an irradiation arrangement with visible reflection microscopy and an IR transmission microscopy systems. The red arrows indicate the direction of the incident laser beam on the sample, while the yellow and green arrows indicate the directions of light from LED1 and LED2, respectively for visible and infrared microscopy imaging. L: lens, M: dielectric mirror, OBJ: objective lens.

profiles with Gaussian distributions, for each irradiation, the applied peak fluence $F$ (at center) is evaluated according to

$$F = \frac{2E}{\pi w_0^2} \tag{1}$$

where $E$ is the pulse energy corresponding to the applied peak power as measured by a detector integrated in the laser source multiplied by the pulse duration. To suitably determine the modification thresholds of the GST sample, the laser power can be varied electronically (computer-controlled for automated experiments). A set of neutral density (ND) filters is also incorporated along the incident laser path. This serves to adjust the pulse energy below the minimal operation level of the laser system ($E \sim$4.4 mJ corresponding to emission at 10% of the maximum energy level).

The inclined irradiation configuration is primarily used to make it possible to implement at normal incidence optical microscopy arrangements for *in-situ* observations of the irradiated zones. An infrared (IR) transmission microscopy arrangement is used for observations of the modified thin films with illumination through the double-side polished Si substrates. It comprises an IR Light-Emitting-Diode (LED) source with a wavelength of 1200 nm positioned behind the sample (see LED2 in Figure 1) and an imaging system based on a microscope objective (Mitutoyo, 5x, NA=0.14, WD=34 mm), a tube lens of focal length 200 mm, and an InGaAs array sensor (Xenics, Bobcat 320). The same microscope objective serves also for observation by visible light reflection microscopy. For this, the system is complemented with an LED source emitting light at a wavelength of 680 nm (see LED1 in Figure 1). Its light is directed onto the sample surface through a non-polarizing

beam splitter (Thorlabs BS013). The beam splitter is transparent for the IR light. Combined with a long-pass dichroic mirror with a cut-off wavelength at 950 nm (Thorlabs, DMLP950), it permits dual-port imaging. The second port uses a CCD camera (Thorlabs CS165MU1) only sensitive to visible light. The different blocks constituting the visible and IR microscopy arrangements are shown by the dashed line boxes in Figure 1.

The sample is mounted on a three-dimensional motorized stage for precise positioning and scanning. The sample is systematically positioned at the best focus of the visible microscope. Given the depth of field of the imaging system, this assures a re-positioning precision on the optical axis of $\pm 40$ µm while we can confirm no noticeable change of the beam size in a range exceeding $\pm 400$ µm (measurement not shown) with the loose focusing conditions used for the laser. For complementary and more detailed analyses, *ex-situ* characterizations are also conducted on the irradiated samples. These include a commercial microscope (Nikon, Eclipse LV100ND) in reflection mode using white-light illumination to reveal potential features inaccessible with the monochromatic red light of the *in-situ* microscope. We have also conducted quantitative phase microscopy measurements using a homemade system. The set-up is identical to the description given in ref.[24] except that the light source is a super-luminescent LED operating at 1317 nm to retrieve directly the refractive index change from transmission images through the silicon substrate. In practice, the system acquires four interference images ($I_k$) with a relative phase delay changing by $\pi/2$ between images. The quantitative phase image is then reconstructed using the equation, $\Delta\phi = \arctan[(I_4 - I_2)/(I_1 - I_3)]$[24]. For detailed spectroscopic analyses, we prepare samples with modified zones of centimetric dimensions. Then, transmittance and reflectance spectra are systematically acquired before and after laser processing. These measurements are compared to simulations (simulation methods described in the next section) of the optical responses depending on sample configurations and possible transitions from amorphous to crystalline state of the different layers. Finally, to confirm the phase transformations, TEM analyses are also conducted after the preparation of nanometric lamellas on selected sample zones by using a focused ion beam (FIB).

## 3. Numerical modeling

### 3.1. Optical properties of GST alloys

The refractive index ($n$) and extinction coefficient ($k$), are the physical quantities that define how materials interact with light and then are the crucial input parameters to describe the measured quantities as the spectral reflectance ($R$) and transmittance ($T$). However, the optical constants for the relatively complex phase change materials considered in this work are inevitably depending on studied conditions. They obviously varies from their composition including the doping materials [25, 26, 27, 28, 29, 30] or stoichiometric fluctuations [31]. Even in the case of identical composition, some works reveal dependencies to the deposition methods [32, 33] and post-processing (e.g. as-deposited amorphous and re-amorphized films [34]). This leads to relatively important dispersion for the reported data in the literature.

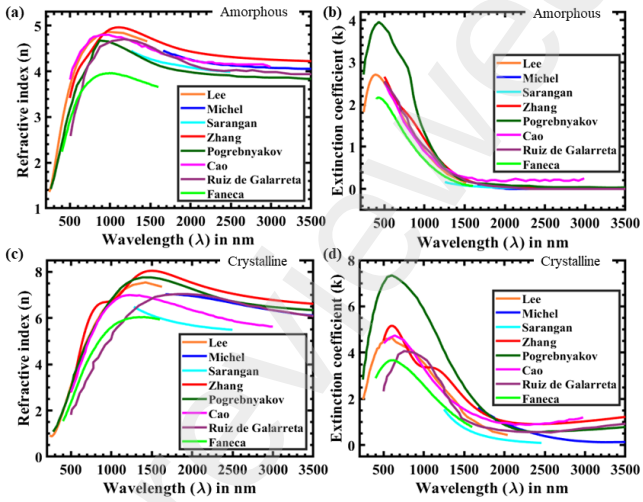


Figure 2: Wavelength dependent optical constants of GST-225 in its different phases reported in various published works [35, 36, 37, 38, 39, 40, 41, 42]. (a) and (b) represent spectral dependency of n and k values for the studied sample in its amorphous state, respectively. (c) and (d) represent the spectral dependency of n and k values for the same material in its crystalline state, respectively.

To illustrate this point and select data for simulations, we present with the Figure 2a-d a range of datasets as found in the literature for the optical constants ($n_{GST}$ and $k_{GST}$) for amorphous (a and b) and crystalline (c and d) states of $Ge_2Sb_2Te_5$ [35, 36, 37, 38, 39, 40, 41, 42]. While all datasets agree on higher refractive indices and extinction coefficients for crystalline state compared to the amorphous form, the comparison of absolute numbers between studies show important variations or even discrepancies. Concentrating on the extinction coefficients, one can note for instance that the value of extinction coefficients from the work of Pogrebnyakov *et al.* [39] are significantly higher than those from other studies.

On the basis of the presentation given in Figure 2, we decided to employ the $n_{GST}$ and $k_{GST}$ values from the study conducted by Lee *et al.* [35] for both the amorphous and crystalline states (orange curves). This dataset has the advantage of fully covering the wavelength range considered in our study (between 600 nm and 1400 nm) and it corresponds to nearly average conditions considering all presented values in Figure 2. To the best of our knowledge, there are no rigorous theoretical treatments and very few experimental studies to describe the effect of Ge enrichment or doping on the optical properties of GST layers [43]. For this reason, we decided to use a simple effective medium approximation method where the optical constants of the GGST doped layers are given by

$$n_{GGST} = a.n_{GST} + b.n_{Ge} + c.n_N \quad (2)$$

$$k_{GGST} = a.k_{GST} + b.k_{Ge} + c.k_N \quad (3)$$

In these expressions, $a$, $b$ and $c$ describe the proportions the different materials and so $a+b+c$=1 for our GGST layers. $n_{Ge}$ and $k_{Ge}$ are the optical constants for pure Ge extracted from

reference [44]. For doping we simply take $n_N = 1$ and $k_N = 0$ corresponding to the assumed properties for a Nitrogen Gas ($N_2$). We expect that such averaging of the values of the constituents that directly make up the composite material is rigorously valid only when the different constituents occupy small separated domains (subwavelength sizes for optical averaging) without complete mixture of the elements and formation of new bonds. For instance, this would mean in this case that the way we account for doping corresponds to porous materials (gas properties). These assumptions clearly deviate from the films studied in our work. Sputtering deposition leads to relatively homogeneous mixtures with atomic bonds between all elements in a dense layer. This aspect is consistent with TEM (see after) and chemical analyses confirming nearly uniformly distributed elements in the deposited layers.

According to these remarks, a specific attention should then be paid to verify the validity of the effective index approximation applied for the studied cases. This corresponds to a part of the preliminary work performed on Sample-0, the simplest configuration without the capping layer. Simulations accounting for the optical constants for the different layers are performed. The properties of the Si substrate are set using the data from reference [45]. The data by Lee *et al.* are directly implemented for the ultrathin amorphous GST layer. The thicker amorphous GGST layer is accounted by taking appropriate material proportions in Eq.2,3 to describe the apparent optical constant values. As we will see later on, an excellent agreement confirms the capacity of the chosen simulation approaches to describe the optical responses of the studied systems.

### 3.2. Multilayer response modeling method and validations

In the context of analyzing the optical responses of a thin-film multilayered structure, the transfer matrix method [46] stands as a fundamental and highly effective technique. This method enables a comprehensive analysis of how light propagates through and interacts with complex layered systems, providing crucial insights into their optical behavior and characteristics, including phenomena like reflection and transmission. It also accounts for potential interference between multiple waves created in the system which is particularly important when considering layers with optical thicknesses comparable to the wavelength. Here, we consider a structure of N stacks of bilayers having 2N+2 interfaces separating 2N+3 media (including substrate and superstrate). Figure 3 represents the schematic of a multilayered structure with 2N+2 interfaces. Then, the transfer matrix $M_{m,m+1}$ serves as a bridge connecting the field component amplitudes between m and m+1 layers.

$$\begin{bmatrix} \vec{E}_{m+1}^{\,\uparrow} \\ \vec{E}_{m+1}^{\,\downarrow} \end{bmatrix} = M_{m,m+1} \times \begin{bmatrix} \vec{E}_{m}^{\,\uparrow} \\ \vec{E}_{m}^{\,\downarrow} \end{bmatrix} \tag{4}$$

$\vec{E}_{m+1}^{\,\uparrow}$ and $\vec{E}_{m}^{\,\downarrow}$ representing the incident and reflected field respectively at the interface, have 3 components along x, y, and z. From Maxwell's equations, the 6× 6 transfer matrix $M_{m,m+1}$

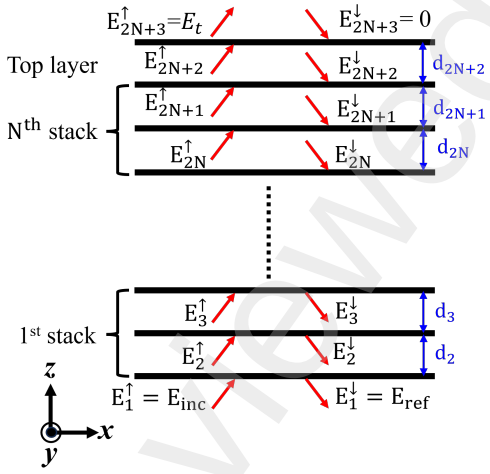


Figure 3: Diagram illustrating the arrangement of a multilayered structure for calculations. Red arrows indicate the electric field directions associated with beam incidence, reflection, and transmission between successive layers. The spacing between consecutive layers is indicated by blue double-sided arrows.

in cartesian coordinate can be written as,

$$\begin{pmatrix}
\frac{\omega_{m+1}+\omega_m}{2\omega_{m+1}}A & 0 & \frac{-k_x(\varepsilon_{m+1}-\varepsilon_m)}{2\omega_{m+1}\varepsilon_{m+1}}A & \frac{\omega_{m+1}-\omega_m}{2\omega_{m+1}}B & 0 & \frac{-k_x(\varepsilon_{m+1}-\varepsilon_m)}{2\omega_{m+1}\varepsilon_{m+1}}B \\
0 & \frac{\omega_{m+1}+\omega_m}{2\omega_{m+1}}A & \frac{-k_y(\varepsilon_{m+1}-\varepsilon_m)}{2\omega_{m+1}\varepsilon_{m+1}}A & 0 & \frac{\omega_{m+1}-\omega_m}{2\omega_{m+1}}B & \frac{-k_y(\varepsilon_{m+1}-\varepsilon_m)}{2\omega_{m+1}\varepsilon_{m+1}}B \\
0 & 0 & \frac{\varepsilon_m\omega_{m+1}+\varepsilon_{m+1}\omega_m}{2\omega_{m+1}\varepsilon_{m+1}}A & 0 & 0 & \frac{\varepsilon_m\omega_{m+1}-\varepsilon_{m+1}\omega_m}{2\omega_{m+1}\varepsilon_{m+1}}B \\
\frac{\omega_{m+1}-\omega_m}{2\omega_{m+1}}A & 0 & \frac{k_x(\varepsilon_{m+1}-\varepsilon_m)}{2\omega_{m+1}\varepsilon_{m+1}}A & \frac{\omega_{m+1}+\omega_m}{2\omega_{m+1}}B & 0 & \frac{k_x(\varepsilon_{m+1}-\varepsilon_m)}{2\omega_{m+1}\varepsilon_{m+1}}B \\
0 & \frac{\omega_{m+1}-\omega_m}{2\omega_{m+1}}A & \frac{k_y(\varepsilon_{m+1}-\varepsilon_m)}{2\omega_{m+1}\varepsilon_{m+1}}A & 0 & \frac{\omega_{m+1}+\omega_m}{2\omega_{m+1}}B & \frac{k_y(\varepsilon_{m+1}-\varepsilon_m)}{2\omega_{m+1}\varepsilon_{m+1}}B \\
0 & 0 & \frac{\varepsilon_m\omega_{m+1}-\varepsilon_{m+1}\omega_m}{2\omega_{m+1}\varepsilon_{m+1}}A & 0 & 0 & \frac{\varepsilon_m\omega_{m+1}+\varepsilon_{m+1}\omega_m}{2\omega_{m+1}\varepsilon_{m+1}}B
\end{pmatrix}$$

Here $\omega_m$ denotes the orthogonal component ($z$) of the wave vector. $k_x$ and $k_y$ are the wave vectors along the x and y directions. The dispersion relation, $\omega_m = \sqrt{\varepsilon_m(4\pi^2/\lambda^2) - k_x^2 - k_y^2}$ incorporates the dielectric permittivity $\varepsilon_m$ of the medium. A and B correspond to the upward and downward propagation operators, respectively. These operators are defined as $A = \exp(i\omega_m d_m)$ and $B = \exp(-i\omega_m d_m)$, where $d_m$ represents the thickness of layer m.

Starting from the topmost layer ($M_{2N+1,2N+2}$, here for TiN) and moving towards the bottom layer ($M_{1,2}$, here for the Si substrate), the overall transfer matrix TT, capturing the entire transformation within the multilayered structure, is computed according to Equation 5.

$$TT = \prod_{m=2N+1}^{1} M_{m,m+1} = M_{2N+1,2N+2} \times M_{2N,2N+1} \ldots . M_{3,2} \times M_{1,2} \tag{5}$$

Consequently, the electric field in the transmission media as a function of the field in the substrate establishes a connection between the field components, facilitating the analysis of light

propagation through the entire multilayered structure.

$$\begin{bmatrix} E_t^x \\ E_t^y \\ E_t^z \\ 0 \\ 0 \\ 0 \end{bmatrix} = \begin{bmatrix} TT_{11} & TT_{12} \\ TT_{21} & TT_{22} \end{bmatrix} \times \begin{bmatrix} E_i^x \\ E_i^y \\ E_i^z \\ E_r^x \\ E_r^y \\ E_r^z \end{bmatrix} \quad (6)$$

In the transmission media, since there are no interfaces present, the reflected components of the electric field are considered to be zero. Therefore, the reflection in this media is disregarded. Both reflected and transmitted fields can then be expressed in terms of the incident one according to:

$$\vec{E}_r = -(TT_{21}^{-1} \times TT_{22})\vec{E}_i \quad (7)$$

$$\vec{E}_t = (TT_{11} - TT_{12} \times TT_{21}^{-1} \times TT_{22})\vec{E}_i \quad (8)$$

These calculations can be rigorously performed for incident light with TE (transverse electric) and TM (transverse magnetic) polarization. In the case of unpolarized light, an average of the reflectance or transmittance values for TE and TM polarizations can be considered. From these field values, we can calculate the overall reflection and transmission coefficients of the structure as it follows,

$$r = \sqrt{|E_{rx}^2| + |E_{ry}^2| + |E_{rz}^2|} \quad (9)$$

$$t = \sqrt{|E_{tx}^2| + |E_{ty}^2| + |E_{tz}^2|} \quad (10)$$

Using Eq.9 and Eq.10, the reflectance ($R = |r|^2$) and transmittance ($T = |t|^2$) can be derived in the general case for diverse multilayered structures.

For the practical cases studied in this work, the light is normal to the interfaces leading to simplifications as TE, TM and unpolarized cases lead to identical results. Our final simulation model also integrates the effect of the substrate (last medium in the above calculation). It accounts for the back surface reflection at the Si-air interface and light absorption within Si in the measured transmitted signals. A modified reflectance formula is considered according to $R' = R + R_{Si} \times (1-R)^2 \exp(-2d_{Si}/\delta)$ where $d_{Si}$, $\delta$ and $R_{Si}$ represent thickness, absorption coefficient and reflectivity of Si substrate respectively. Similarly, a modified transmittance is calculated to account for the attenuation of the light as it passes through the silicon substrate. It is given by $T' = T \times T_{Si} \exp(-d_{Si}/\delta)$ where $T_{Si}$ stands for the transmission at the Si-air interface. Obviously, all these calculations can be used to describe the spectral response by considering the wavelength dependence of the different input parameters (index, extinction coefficients). To validate the numerical model, we compare calculations with measurements using the UV-NIR spectrometer for Type-0 sample with $t = 50$ nm (hereafter simply called Sample-0).

The Figure 4 presents the obtained results. The calculations use the above mentioned data for the amorphous sample (red dashed line). The measurements (continuous red line) are performed on films as they are deposited (no irradiation). An excellent agreement is revealed between the spectroscopic and

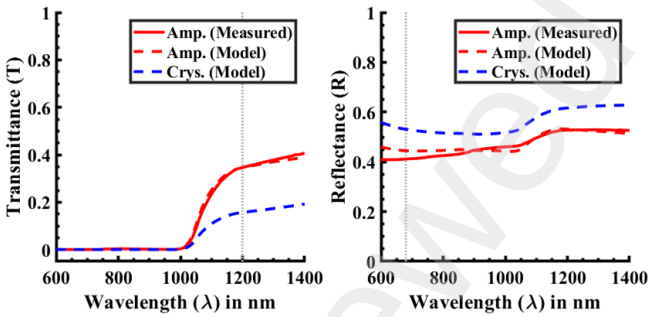


Figure 4: Transmittance (left) and reflectance (right) characteristics of amorphous and crystalline phases of Sample-0 (Type-0, $t = 50$ nm) with a comparative study between simulation and UV spectroscopy showing good agreement. Expected characteristic changes of transmittance and reflectance values for the crystalline state are estimated theoretically. The terms 'Amp.' and 'Crys.' stand for the amorphous and crystalline states of the sample.

simulation data for the amorphous case (red curves) indicating that the optical properties of the different layers are likely properly accounted and with the validity of the applied simplifications for the simulations.

On the basis of this validity demonstration, one can interestingly predict the expected changes with the crystallization of GST layers. For that, we simply need to replace the optical constants for amorphous GST by those for crystalline GST (data sets from ref.[35] as discussed before) in our simulations. The results are displayed on the same graph (dashed blue line). From these and previous calculation results, we note that the transmittance is measurable only for wavelengths above 1.1 µm. This corresponds to the absorption edge of silicon and then confirms that we are dealing with transparent films (without capping). Interestingly, by comparing red and blue curves, we expect that the phase transition from amorphous to crystalline must lead to a drop in the sample transmittance in the infrared domain and an increase in sample reflectance in a broad range of wavelengths. However, we can immediately note a relative change higher in transmittance (typ. -50%) in comparison to reflectance signals (typ. +20%) which tends to reveal a potential improved sensitivity using infrared diagnostics for optical detection of film crystallization. However, in comparison to this sample configuration used for validity demonstrations, the main studied samples have an additional TiN capping layer. The large values of the extinction coefficients of TiN at 1070 nm (see before) and other NIR wavelengths may then cause limitations for transmission detection that will be further evaluated with the investigations on Type-1 and Type-2 samples.

## 4. Results and Discussions

In the quest for suitable conditions for controllable phase changes of GST using laser irradiations, previous studies have mainly explored shorter pulse duration ranging from femtosecond to nanosecond regimes [7, 8, 9, 10, 11, 12, 13, 14, 15, 16, 17]. Most of these works also considered single GST layers on top of substrates. Taken together, all these works demon-

strate the capacity to amorphize or crystallize layers depending on laser conditions. Even if contradictions still persist, the shortest pulses leads to ultrafast quenching conditions shown as more favorable to achieve amorphization and the longest pulses lead to more appropriate temperature responses to obtain well defined crystallized layers. In this work, we add the difficulty of multilayer PCM systems. These systems are more commonly studied with conventional thermal annealing methods (in furnace). In this context, we have decided to concentrate on the problem of crystallization from as-deposited amorphous films. To approach steady-state thermal annealing conditions for comparisons with previous works, we have decided to use relatively long laser pulses. This is an important step to validate the laser method before tentatively addressing the complexities of out-of-equilibrium material responses using ultrashort pulses in future works.

Looking for optimized laser parameters for crystallization, we present the results obtained on the thinnest Type-1 and Type-2 ($t = 50$ nm, composition details in table 1) samples (hereafter simply called Sample-1 and Sample-2) with 50-µs single pulse at varying fluence ($F$) levels. The modified areas on the irradiated samples are systematically observed and analyzed using *in-situ* and *ex-situ* optical microscopy techniques described in section 2.2. The captured images with the different microscopes are presented together in Figure 5 for comparisons between observation modes. The Figure also presents the results obtained for Sample-1 (Figure 5a) and for Sample-2 (Figure 5b) to visualize differences in sample responses. A first conclusion from these observations is a laser fluence threshold for modification ($F_{th}$) modestly higher for Sample-1 ($\sim 11.9$ J/cm$^2$) than for Sample-2 ($\sim 10.8$ J/cm$^2$). Assuming similar heating sources (TiN layer), this must indicate sensitive layers closer to the heat source and/or less efficient heat dissipation with the multilayer configuration of Sample-2.

Concentrating on the apparent contrasts for the different images, it is also important to emphasize that the modifications near threshold conditions ($F \approx F_{th}$) are hardly distinguishable with reflection microscopy images (visible light) and even more so for Sample-1 in comparison to Sample-2. In contrast, the IR transmission images, despite being based on more noisy and performance-limited sensor technologies (InGaAs arrays) exhibit a relative change in the transmittance signals more visible and measurable. This shows the importance of investigating different spectral domains which are not performing equally to define the best detection schemes. These observables here immediately confirm the previously observed superiority of the infrared transmittance diagnostic (Sample-0) even in the presence of the TiN layer (Sample-1 and Sample-2).

Remarkably, for both samples, we observe for conditions just above the threshold a relative drop in sample IR transmittance. We also note an inverted contrast between the monochromatic visible microscope image (bright spot) and the corresponding IR microscope image (see for instance the two bottom images at 10.8 J/cm$^2$ in Figure 5b). This is already qualitatively consistent with the transition from the amorphous to the crystalline phase leading to increased IR absorption of the layers as discussed before for Sample-0. For larger fluence values, independently to imaging techniques, we note progressively forming concentric rings. Given the Gaussian irradiation profile, this can be attributed to different material modifications at different energy density levels but also interference effects between the waves reflected at the multiple interfaces of the progressively modified layers (so-called Newton rings). Thin-film interference are very likely contributing modestly to this feature given the thickness of the considered layers which are only a small fraction of the applied wavelengths. Ultimately, the highest presented fluence levels have caused ablation of the films (e.g. $F = 17.4$ J/cm$^2$ in Figure. 5a) as confirmed by SEM characterizations. The last presented optical images in Figure 5 for both samples show clearly uneven damages contrasting with well defined relatively uniform concentric ring transformations obtained at lower fluences. One can also remark on debris redeposition of ablated film materials in these images. Between the first modification at $F_{th}$ and these ablation features various modification regimes are produced. However, SEM analyses have also revealed film morphology changes at fluence $F > 14.7$ J/cm$^2$ for Sample-1 and $F > 13$ J/cm$^2$ for Sample-2, corresponding in both cases to a fluence level where we observe a change from a central local darkening to a brightening in infrared transmission. For this reason, we decided to concentrate hereafter the analyses on the near threshold conditions corresponding to the first detectable darkening of the sample in IR transmission.

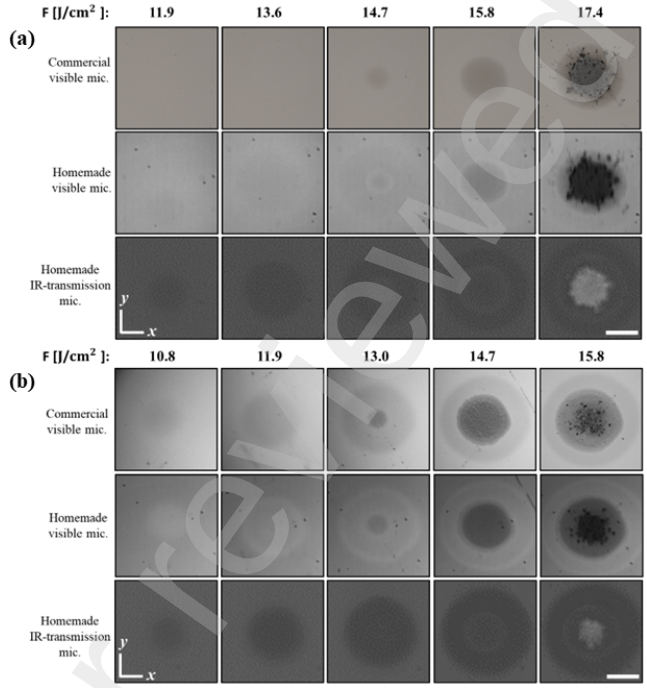


Figure 5: Microscopy images of – (a) sample-1 and (b) sample-2 after 50-µs single-shot irradiation at varying fluence ($F$) levels. The modification thresholds ($F_{th}$) are found at $\sim$11.9 J/cm$^2$ and $\sim$10.8 J/cm$^2$ for sample-1 and sample-2, respectively. The top, middle, and bottom rows display the images by *ex-situ* visible reflection microscopy (commercial system), *in-situ* monochromatic reflection (at 680 nm) microscopy and *in-situ* IR transmission (at 1200 nm) microscopy (home-made systems), respectively. Scale bar is 100 µm.

For in-depth investigations of the laser-modified zones in-

cluding spectroscopy and TEM analyses for atomic-level information, it was necessary to prepare modified films on areas larger than those produced by single-shot irradiations. For this we rely on a scanning procedure as described in Figure 6a. In practice, we apply the same 50-µs pulses at fluence $F$ = 12.4 J/cm$^2$ and operate the source at the repetition rate of 10 Hz while moving the sample along parallel lines at a constant velocity of 1.4 mm/s. With consecutive lines separated by 0.14 mm, we then obtain a desired beam overlapping of about 77% in both considered directions [47]. This corresponds to pre-determined conditions to obtain relatively uniform processing. Using this procedure, we prepared laser-modified zones exceeding $10 \times 10$ mm$^2$ on both types of samples (Sample-1 and Sample-2).

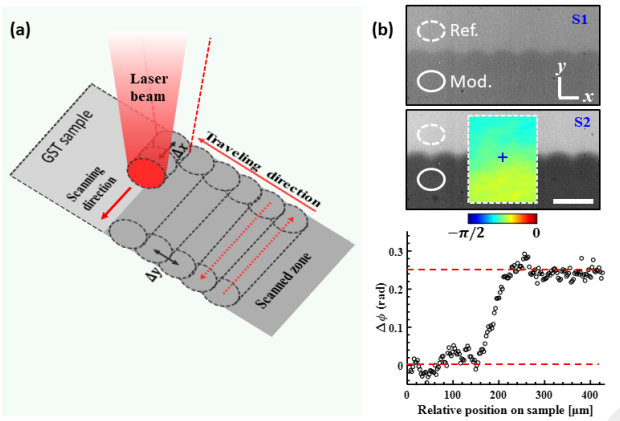


Figure 6: (a) Schematic illustration of the laser-scanning procedure for large-area transformations of the films, where Δx and Δy are the center-to-center separations between the successive irradiation spots along $x$– and $y$–axis, respectively. (b) IR transmission microscopy images of Sample-1 (S1) and Sample-2 (S2), laser-scanned with 50-µs single pulse irradiation at $F$ = 12.4 J/cm$^2$. Inset represents the phase image of Sample-2. The '+' sign indicates the position where a vertical line profile analysis is performed and presented below. The distance between two red dotted lines represents the $\Delta\phi$ value between unmodified and modified zone. The scale bar is 200 µm.

The two processed samples are then analysed by all available optical methods for this work (incl. spectroscopy). The Figure 6b shows the edge of the processed zones for both samples by IR transmission microscopy. As expected, a relatively uniform darkening of the samples is observed on the processed regions even if Sample-2 exhibits a larger relative change of the transmission signals. Because all optical characteristics of the processed films are consequences of optical constants, we first complemented the IR amplitude imaging by quantitative phase imaging on the same sample region. This is expected to reveal the obtained relative refractive index change for a direct, model-independent comparison with the used database for GST materials. Due to the sensitivity limit of our phase microscopy arrangement, a reliable measurement has been only possible for Sample-2 giving sufficiently large optical phase modulations. For Sample-1, the optical phase change was significantly lower on the order of the noise level resulting from the four-step acquisition procedure (see section 2.2.). The inset of Figure 6b displays the retrieved phase image (in color scale) of the laser-scanned region, revealing two distinct phase levels between the modified and unmodified regions. According to a profile analysis along a line perpendicular to the edge of the processed zone also presented at the bottom of Figure 6b, the phase signal exhibits a step which reveals a positive phase change of $\Delta\phi \approx 0.25$ rad with laser processing. From this phase level, we can extract the corresponding change of refractive index using the equation $\Delta n = \lambda\Delta\phi/2\pi d$ with $d$ the thickness of the modified layer. By taking $d$ = 50 nm being the total thickness of the expected active GST layers for our samples, we obtain a positive refractive index change of $\Delta n \sim 1$. For comparison, the data from Lee *et al.* [35] used in this work expect a change from $n = 4.8$ to $n = 7$ with GST crystallization, corresponding to $\Delta n \sim 2$. Accordingly, we note that this measurement gives a correct order of magnitude but a significant deviation. This could be immediately attributed to specificities from our sample compositions but, as we will show later on, it is mainly explained by an improper thickness value taken for the active layer in this first estimation.

For detailed optical response analyses, we turn to spectroscopy using the same UV-IR spectrometer as for Sample-0. The spectral measurements for both Sample-1 and Sample-2 are shown in Figure 7 where we present the transmittance and reflectance for the reference materials (continuous red) taken in a non-modified zone and for the laser-processed region (continuous blue). For comparisons, we also run simulations using the optical constants as described previously in the case of GST layers totally amorphous (dashed red) and totally crystallized (dashed blue). Considering specifically the microscopy wavelengths (shown by grey lines on graphs of Figure 7), for Sample-1, the relative changes induced by laser processing on the transmittance (at 1200 nm) and reflectance (at 680 nm) values are measured at $\Delta T_{rel} \simeq$ -19% and $\Delta R_{rel} \simeq$ -3% which correspond well with the microscopy images. However, it is in contradiction with the simulations assuming the crystallization of the GST films as we expect in this case $\Delta T_{rel}^{sim.}$ = -53% and $\Delta R_{rel}^{sim.}$ = +12%. We note in this case that for the reflectance not only the magnitude but also the sign of the relative variation disagree. In the case of Sample-2, we obtain a better agreement. The measurements give $\Delta T_{rel} \simeq$ -64% and $\Delta R_{rel} \simeq$+6% while the estimates from the simulation lead to $\Delta T_{rel}^{sim.}$ = -67% and $\Delta R_{rel}^{sim.}$ =+18%. While some indication of GST phase change from the amorphous to the crystalline state can be attributed qualitatively from these comparative analyses, noticeable differences persist between our expectations and observations for both samples (e.g. reflectance magnitude for Sample-2 ). These discrepancies must reveal inappropriate assumptions on material configurations in the model. These leads us to advanced material analyses for further advances and improvements of the models.

In the Figure 8 we show TEM images of the multilayer system after lamella preparation in laser-scanned area of Sample-2. First, the cross-sections confirm that the geometrical characteristics of the stacks including the typical 5-nm thickness for the thinnest deposited layers are maintained after laser processing. However the images reveal very interestingly a selective processing where only the GST layers are transformed into crystals while the GGST layers remain amorphous after

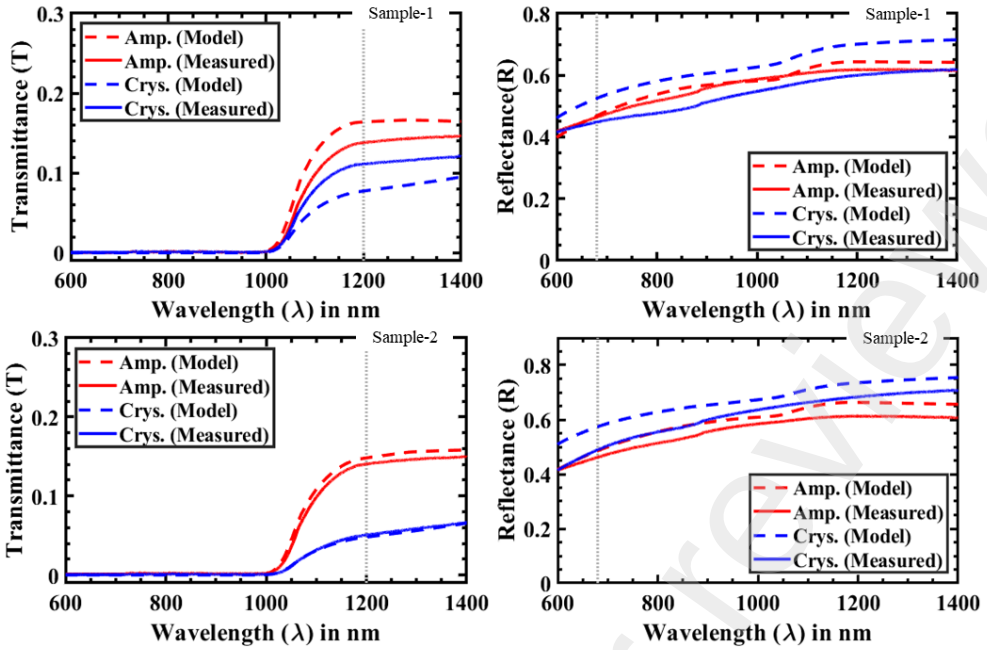


Figure 7: Transmittance and reflectance spectra of the studied samples. The measured spectra are for reference (non-modified) and laser-processed zones (solid lines). A comparison is made with simulations under the assumption that the GST layers are initially fully amorphous and processed regions result in totally crystallized materials (dashed lines). Despite relatively good agreement for the transmittance spectra of Sample-2 important discrepancies persist for the other presented spectra.

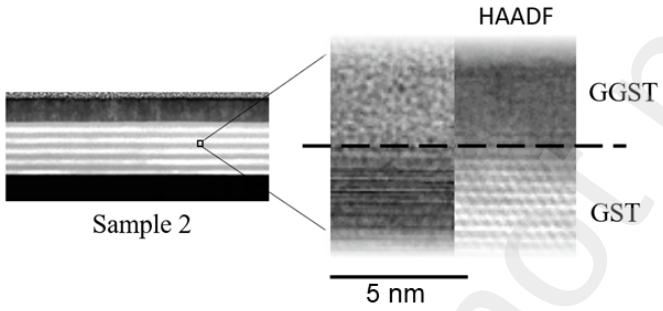


Figure 8: TEM analysis Sample-2 revealing selective crystallization of GST layers in the laser-processed zones. A single interface between GGST and GST layers is shown to confirm the crystalline state of GST after laser treatment. HAADF stands for High-angle annular dark-field imaging.

laser irradiation. Similar observations are on sample 1 where only the GST underlayer is selectively crystallised. While the detailed Materials Science questions will be the subject of a future paper, it is striking to note the high-quality large monocrystals formed with the applied laser conditions. The results also confirm distincts and well defined crystallization thresholds for GST and GGST layers and that we applied here laser conditions between these thresholds. This deviates from the literature where mixed layers due to the important mobilities of elements under thermal stimulations and poly-crystalline forms are more commonly reported for GST.

The observed partial and selective crystallization significantly deviates from our previous considerations with a model intended to describe the change of the optical properties assuming a crystallization of all potentially active layers (incl. GST and GGST layers). On the basis of this observation, we can re-adjust the multilayer model accounting for a change on the optical constants of GST layers only while maintaining the same constants for GGST. Accordingly, the properties in the TMM model is only modified for a single 5-nm-thick layer for Sample-1 and 5 layers in Sample-2 corresponding to a total of 25-nm of GST. Immediately at this stage, this means that the active layer of 25 nm instead of 50 nm for Sample-2 must result in a twofold increase for the relative index variation retrieved from the phase microscopy measurement. More precisely, the $\Delta\phi$ derived above (Figure 6) must be actually interpreted as corresponding to $\Delta n \sim 2$ which now compares very favorably with the data of Lee *et al.* [35] used for this work (Figure 2).

The changes in the spectroscopic data with this model correction are presented in Figure 9. While we can still note remaining imperfections, in comparison to the results presented in Figure 8, a significantly improved agreement is now obtained between measurements and simulations. As an illustration, the sign error on the relative change of reflectance observed for Sample-1 in Figure 8 is now corrected as the crystallized sample now exhibits as a slightly higher reflectance than its amorphous analog in the visible part of the spectrum for both the measurements and simulations. The improved agreement showing a model that accounts now properly for the main aspects behind the optical response of the systems can be assessed clearly by comparing the results obtained at the two wavelengths used for microscopy imaging (see vertical grey lines on Figure 9). These results are summarized in table 2 where the measured relative changes in reflectance and transmittance with processing are given for both samples

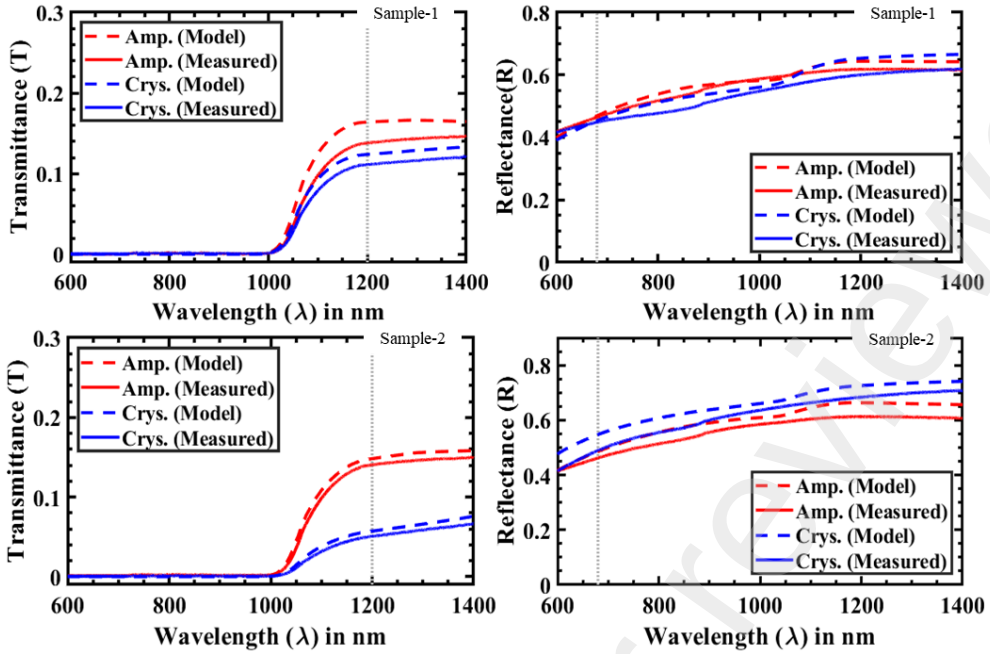


Figure 9: Transmittance and reflectance of the studied samples. The measured spectra are for reference (non-modified) and laser-processed zones (solid lines, red and blue respectively). A comparison is made with simulations under the assumption that the GST layers are initially fully amorphous and processed regions result in partially crystallized materials (dashed lines) that are stacks where only GST layers are crystallized (not the GGST layers).

and compared to both model configurations. Assuming partial crystallization (GST layers only), we predict with simulations $-24\%$ and $-61\%$ transmittance drops at 1200 nm for Sample-1 and Sample-2, respectively, which aligns well with the spectral measurements ($-19\%$ and $-64\%$ respectively). The main discrepancies with reflectance measurements are also now solved. For Sample-1, both the simulation and spectroscopy results show a reflectance drop of $-3\%$ while an increase of $+12\%$ was predicted under the assumption of a total crystallization (GST and GGST layers).

| Case | | $\Delta T_{rel}(\%)$ | | $\Delta R_{rel}(\%)$ | |
|---|---|---|---|---|---|
| Assumption | Sample | Sim. | Meas. | Sim. | Meas. |
| Full crys.: | Sample-1 | -53 | -19 | +12 | -3 |
| | Sample-2 | -67 | -64 | +18 | +6 |
| Partial crys.: | Sample-1 | -24 | -19 | -3 | -3 |
| | Sample-2 | -61 | -64 | +12 | +6 |

Table 2: Summary of measured and simulated relative change of transmittance $\Delta T_{rel}$ and reflectance $\Delta R_{rel}$ at 1200 nm and 680 nm respectively as caused by laser processing on the two types of samples for this work. For comparisons, the results of simulations assuming total or partial crystallization are given. All the values here are presented in % according to the expressions $\Delta T_{rel} = (T_{crys} - T_{amp})/(T_{amp})$ and $\Delta R_{rel} = (R_{crys} - R_{amp})/(R_{amp})$. Sim. and Meas. correspond to simulation and spectroscopy measurements, respectively, providing a comprehensive perspective on the material transformations under consideration.

Beside the demonstration of a valid model made with these comparisons, important conclusions can be derived from the measurements of the response of these model systems. First, the significant difference found on the relative transmittance changes between Sample-1 and Sample-2 at the same processing fluence level ($\sim$ 12.4 J/cm$^2$) can be attributed to their distinct layered structures. The highest change for Sample-2 can be directly inferred to a signal that integrates a larger amount of crystallized materials (5 layers of GST instead of 1 for Sample-1). After these considerations, it is important to highlight that relative transmittance change at 1200 nm for Sample-1 remains relatively large (measured at $-19\%$) and it is easily detectable as confirmed by the microscopy results (see Figure 5). This is remarkable in view of the 5-nm thin layer transformed in this case. This result may first appear counter-intuitive in view of expected limitations for optical detection. However, the results also confirm wavelength and detection schemes not performing equally as the relative change in visible reflectance is only found at only $-3\%$ which can become much more challenging to image with standard dynamic cameras as the one used in this work (see also the comparison between visible and infrared images in Figure 5). Accordingly, we identify infrared transmission microscopy at near-band edge absorption of silicon (1200 mn) as a configuration very optimal for sensitive detection of phase change in ultrathin GST layers. Such configuration is already implemented in our current setup (see Figure 1) and must serve for *insitu* monitoring for future work aiming at laser annealing studies under varying irradiation parameters.

## 5. Summary and conclusions

In this work, we have concentrated on optically inducing and probing the crystallization of GST thin-film systems. The melt-

ing and subsequent re-solidification conditions driven by irradiation with 50-µs laser pulses is shown as appropriate to selectively crystallize GST layers while leaving unaffected some other Ge-rich GST layers. This selective processing can be directly correlated with the higher temperature threshold conditions for GGST. The phase change of GGST is also likely accessible by laser irradiation but higher laser fluence conditions also caused morphological changes and/or damages on the studied samples.

On the basis of investigations using different optical techniques, and systematic comparisons of the measured optical responses, we made a critical analysis of the data sets available in the literature to describe the optical constant of GST materials. Applying the TTM to simulate spectroscopic response of the thin-film systems, we have validated a data set and the effective medium approximation as an appropriate method to account for the different properties of the layers with different compositions. Examining the irradiated materials with the different methods, we conclude on a decisive superiority of infrared transmission diagnostics ($\lambda > 1200$ nm) for the detection of phase changes in GST layers. Transmission microscopy at 1200 nm as implemented in the current version of our setup gives the ability to detect the phase change of ultra-thin layers (down to 5 nm) and locally induced by single-shot irradiation. These developments must serve for the advent of new and efficient methods, complementing advanced material analysis methods for the study of the behavior of this important phase change materials.

## 6. Acknowledgement

The research leading to these results has received funding from the French PACA (Provence-Alpes-Cote d'Azur) Regional Council (2022 Grants: INTENSITY). It has been conducted using LaMP facilities at LP3.

## 7. Conflicts of interest

The authors declare no conflicts of interest.

## References

[1] Stanford R. Ovshinsky. "Reversible Electrical Switching Phenomena in Disordered Structures". In: *Phys. Rev. Lett.* 21 (20 Nov. 1968), pp. 1450–1453. DOI: 10.1103/PhysRevLett.21.1450.

[2] David Loke et al. "Breaking the speed limits of phase-change memory". In: *Science* 336.6088 (2012), pp. 1566–1569. DOI: 10.1126/science.1221561.

[3] A. Pirovano et al. "Reliability study of phase-change nonvolatile memories". In: *IEEE Transactions on Device and Materials Reliability* 4.3 (2004), pp. 422–427. DOI: 10.1109/TDMR.2004.836724.

[4] Zhe Yang, Yi Li, and Xiangshui Miao. "13 - Chalcogenide materials for optoelectronic memory and neuromorphic computing". In: *Photo-Electroactive Nonvolatile Memories for Data Storage and Neuromorphic Computing*. Ed. by Su-Ting Han and Ye Zhou. Woodhead Publishing Series in Electronic and Optical Materials. Woodhead Publishing, 2020, pp. 293–315. ISBN: 978-0-12-819717-2. DOI: https://doi.org/10.1016/B978-0-12-819717-2.00013-8.

[5] Kang Zhou et al. "Phase change of Ge2Sb2Te5 under terahertz laser illumination". In: *APL Materials* 9.10 (2021). DOI: https://doi.org/10.1063/5.0070304.

[6] Wenju Zhou et al. "Transient study of femtosecond laser–induced Ge2Sb2Te5 phase change film morphology". In: *Micromachines* 12.6 (2021), p. 616. DOI: https://doi.org/10.3390/mi12060616.

[7] V Weidenhof et al. "Laser induced crystallization of amorphous Ge 2 Sb 2 Te 5 films". In: *Journal of applied physics* 89.6 (2001), pp. 3168–3176. DOI: http://dx.doi.org/10.1063/1.1351868.

[8] V Weidenhof et al. "Atomic force microscopy study of laser-induced phase transitions in Ge 2 Sb 2 Te 5". In: *Journal of applied physics* 86.10 (1999), pp. 5879–5887. DOI: https://doi.org/10.1063/1.371606.

[9] Noboru Yamada et al. "Rapid-phase transitions of GeTe-Sb2Te3 pseudobinary amorphous thin films for an optical disk memory". In: *Journal of Applied Physics* 69.5 (1991), pp. 2849–2856. DOI: https://doi.org/10.1063/1.348620.

[10] J Siegel et al. "Rewritable phase-change optical recording in Ge 2 Sb 2 Te 5 films induced by picosecond laser pulses". In: *Applied physics letters* 84.13 (2004), pp. 2250–2252. DOI: https://doi.org/10.1063/1.1689756.

[11] Jan Siegel et al. "Amorphization dynamics of Ge2Sb2Te5 films upon nano-and femtosecond laser pulse irradiation". In: *Journal of Applied Physics* 103.2 (2008). DOI: http://dx.doi.org/10.1063/1.2836788.

[12] Y Liu et al. "Crystallization of Ge2Sb2Te5 films by amplified femtosecond optical pulses". In: *Journal of applied physics* 112.12 (2012). DOI: https://doi.org/10.1063/1.4770359.

[13] Guangjun Zhang et al. "Crystallization of amorphous Ge2Sb2Te5 films induced by a single femtosecond laser pulse". In: *Solid state communications* 133.4 (2005), pp. 209–212. DOI: https://doi.org/10.1016/j.ssc.2004.11.013.

[14] Kotaro Makino, Junji Tominaga, and Muneaki Hase. "Ultrafast optical manipulation of atomic arrangements in chalcogenide alloy memory materials". In: *Optics express* 19.2 (2011), pp. 1260–1270. DOI: https://doi.org/10.1364/OE.19.001260.

[15] Rebecca L Cotton and Jan Siegel. "Stimulated crystallization of melt-quenched Ge2Sb2Te5 films employing femtosecond laser double pulses". In: *Journal of Applied Physics* 112.12 (2012). DOI: https://doi.org/10.1063/1.4770493.

[16] Hongbing Lu et al. "Single Pulse Laser-Induced Phase Transitions of PLD-Deposited Ge2Sb2Te5 Films". In: *Advanced Functional Materials* 23.29 (2013), pp. 3621–3627. DOI: https://doi.org/10.1002/adfm.201202665.

[17] Xinxing Sun et al. "Crystallization of Ge2Sb2Te5 thin films by nano- and femtosecond single laser pulse irradiation". In: *Scientific Reports* 6 (June 2016), p. 28246. DOI: 10.1038/srep28246.

[18] SK Sundaram and Eric Mazur. "Inducing and probing non-thermal transitions in semiconductors using femtosecond laser pulses". In: *Nature materials* 1.4 (2002), pp. 217–224. DOI: https://doi.org/10.1038/nmat767.

[19] Paola Zuliani et al. "Engineering of chalcogenide materials for embedded applications of Phase Change Memory". In: *Solid-State Electronics* 111 (2015), pp. 27–31. DOI: https://doi.org/10.1016/j.sse.2015.04.009.

[20] O Thomas et al. "Crystallization behavior of N-doped Ge-rich GST thin films and nanostructures: An in-situ synchrotron X-ray diffraction study". In: *Microelectronic Engineering* 244 (2021), p. 111573. DOI: https://doi.org/10.1016/j.mee.2021.111573.

[21] Minh Anh Luong et al. "Impact of nitrogen on the crystallization and microstructure of Ge-rich GeSbTe alloys". In: *physica status solidi (RRL)–Rapid Research Letters* 15.3 (2021), p. 2000443. DOI: https://doi.org/10.1002/pssr.202000443.

[22] Marta Agati et al. “Effects of surface oxidation on the crystallization characteristics of Ge-rich Ge-Sb-Te alloys thin films”. In: *Applied Surface Science* 518 (2020), p. 146227. DOI: https://doi.org/10.1016/j.apsusc.2020.146227.

[23] Leonid Yu Beliaev et al. “Optical properties of plasmonic titanium nitride thin films from ultraviolet to mid-infrared wavelengths deposited by pulsed-DC sputtering, thermal and plasma-enhanced atomic layer deposition”. In: *Optical Materials* 143 (2023), p. 114237. DOI: https://doi.org/10.1016/j.optmat.2023.114237.

[24] Q Li et al. “Quantitative-phase microscopy of nanosecond laser-induced micro-modifications inside silicon”. In: *Applied optics* 55.33 (2016), pp. 9577–9583. DOI: https://doi.org/10.1364/AO.55.009577.

[25] Hun Seo Hun Seo et al. “Investigation of crystallization behavior of sputter-deposited nitrogen-doped amorphous Ge2Sb2Te5 thin films”. In: *Japanese Journal of Applied Physics* 39.2S (2000), p. 745. DOI: 10.1143/JJAP.39.745.

[26] Xilin Zhou et al. “Carbon-doped Ge2Sb2Te5 phase change material: A candidate for high-density phase change memory application”. In: *Applied Physics Letters* 101.14 (2012). DOI: https://doi.org/10.1063/1.4757137.

[27] S Privitera, E Rimini, and R Zonca. “Amorphous-to-crystal transition of nitrogen-and oxygen-doped Ge2Sb2Te5 films studied by in situ resistance measurements”. In: *Applied physics letters* 85.15 (2004), pp. 3044–3046. DOI: https://doi.org/10.1063/1.1805200.

[28] Guoxiang Wang et al. “Improved thermal and electrical properties of Al-doped Ge2Sb2Te5 films for phase-change random access memory”. In: *Journal of Physics D: Applied Physics* 45.37 (2012), p. 375302. DOI: 10.1088/0022-3727/45/37/375302.

[29] SJ Wei et al. “Phase change behavior in titanium-doped Ge2Sb2Te5 films”. In: *Applied Physics Letters* 98.23 (2011). DOI: https://doi.org/10.1038/nmat2009.

[30] Keyuan Ding et al. “Study on the Cu-doped Ge2Sb2Te5 for low-power phase change memory”. In: *Materials Letters* 125 (2014), pp. 143–146. ISSN: 0167-577X. DOI: https://doi.org/10.1016/j.matlet.2014.03.180.

[31] Matthias Wuttig and Noboru Yamada. “Phase-change materials for rewriteable data storage”. In: *Nature materials* 6.11 (2007), pp. 824–832. DOI: https://doi.org/10.1038/nmat2009.

[32] Iosif-Daniel Simandan et al. “Influence of deposition method on the structural and optical properties of Ge2Sb2Te5”. In: *Materials* 14.13 (2021), p. 3663. DOI: https://doi.org/10.3390%2Fma14133663.

[33] Henning Dieker and Matthias Wuttig. “Influence of deposition parameters on the properties of sputtered Ge2Sb2Te5 films”. In: *Thin Solid Films* 478.1 (2005), pp. 248–251. ISSN: 0040-6090. DOI: https://doi.org/10.1016/j.tsf.2004.08.019.

[34] Pramod K Khulbe, Ewan M Wright, and Masud Mansuripur. “Crystallization behavior of as-deposited, melt quenched, and primed amorphous states of $Ge_2$ $Sb_{2.3}$ $Te_5$ films”. In: *Journal of Applied Physics* 88.7 (2000), pp. 3926–3933. DOI: https://doi.org/10.1063/1.1289811.

[35] Bong-Sub Lee et al. “Investigation of the optical and electronic properties of Ge2Sb2Te5 phase change material in its amorphous, cubic, and hexagonal phases”. In: *Journal of Applied Physics* 97.9 (2005). DOI: https://doi.org/10.1063/1.1884248.

[36] Ann-Katrin U Michel, Matthias Wuttig, and Thomas Taubner. “Design parameters for phase-change materials for nanostructure resonance tuning”. In: *Advanced Optical Materials* 5.18 (2017), p. 1700261. DOI: http://dx.doi.org/10.1002/adom.201700261.

[37] Andrew Sarangan et al. “Broadband Reflective Optical Limiter Using GST Phase Change Material”. In: *IEEE Photonics Journal* 10.2 (2018), pp. 1–9. DOI: 10.1109/JPHOT.2018.2796448.

[38] Yifei Zhang et al. “Broadband transparent optical phase change materials for high-performance nonvolatile photonics”. In: *Nature communications* 10.1 (2019), p. 4279. DOI: https://doi.org/10.1038/s41467-019-12196-4.

[39] Alexej V Pogrebnyakov et al. “Reconfigurable near-IR metasurface based on Ge 2 Sb 2 Te 5 phase-change material”. In: *Optical Materials Express* 8.8 (2018), pp. 2264–2275. DOI: https://doi.org/10.1364/OME.8.002264.

[40] Tun Cao et al. “Giant enhancement of third harmonic generation from Ge2Sb2Te5 based Fabry-Perot cavity”. In: *arXiv preprint arXiv:1901.08795* (2019). DOI: https://doi.org/10.48550/arXiv.1901.08795.

[41] C Ruiz de Galarreta et al. “Tunable optical metasurfaces enabled by chalcogenide phase-change materials: from the visible to the THz”. In: *Journal of Optics* 22.11 (2020), p. 114001. DOI: 10.1088/2040-8986/abbb5b.

[42] Joaquin Faneca et al. “Performance characteristics of phase-change integrated silicon nitride photonic devices in the O and C telecommunications bands”. In: *Optical Materials Express* 10.8 (2020), pp. 1778–1791. DOI: https://doi.org/10.1364/OME.397833.

[43] SMS Privitera et al. “Crystallization properties of melt-quenched Ge-rich GeSbTe thin films for phase change memory applications”. In: *Journal of Applied Physics* 128.15 (2020). DOI: https://doi.org/10.1063/5.0023696.

[44] Tatiana Amotchkina et al. “Characterization of e-beam evaporated Ge, YbF3, ZnS, and LaF3 thin films for laser-oriented coatings”. In: *Appl. Opt.* 59.5 (Feb. 2020), A40–A47. DOI: 10.1364/AO.59.000A40.

[45] Carsten Schinke et al. “Uncertainty analysis for the coefficient of band-to-band absorption of crystalline silicon”. In: *Aip Advances* 5.6 (2015). DOI: https://doi.org/10.1063/1.4923379.

[46] Fadi I Baida and Maria-Pilar Bernal. “Correcting the formalism governing Bloch Surface Waves excited by 3D Gaussian beams (Supporting documents)”. In: *Communications Physics* 3.1 (2020), p. 86. DOI: https://doi.org/10.1038/s42005-020-0349-8.

[47] Jorge Ramos and David Bourell. “Mechanics of the selective laser raster-scanning surface interaction”. In: *2003 International Solid Freeform Fabrication Symposium*. 2003. DOI: http://dx.doi.org/10.26153/tsw/5616.